Journal of Energy Chemistry 77 (2023) 317–325

Contents lists available at ScienceDirect

Journal of Energy Chemistry

journal homepage: www.elsevier.com/locate/jechem

http://www.journals.elsevier.com/journal-of-energy-chemistry/

# Ligand-free $CsPbBr_3$ with calliandra-like nanostructure for efficient artificial photosynthesis

Yan-Fei Mu [a,b], Hui-Ling Liu [a], Meng-Ran Zhang [a], Hong-Juan Wang [a], Min Zhang [a,*], Tong-Bu Lu [a,*]

[a] MOE International Joint Laboratory of Materials Microstructure, Institute for New Energy Materials and Low Carbon Technologies, School of Materials Science and Engineering, Tianjin University of Technology, Tianjin 300384, China
[b] School of Chemistry and Chemical Engineering, Yangzhou University, Yangzhou 225009, Jiangsu, China

ARTICLE INFO

*Article history:*
Received 11 August 2022
Revised 10 October 2022
Accepted 17 October 2022
Available online 25 October 2022

*Keywords:*
Artificial photosynthesis
Charge separation
Halide perovskite
Ligand-free
Vacancy defect

ABSTRACT

The low-efficiency $CO_2$ uptake capacity and insufficient photogenerated exciton dissociation of current metal halide perovskite (MHP) nanocrystals with end-capping ligands extremely restrict their application in the field of artificial photosynthesis. Herein, we demonstrate that ligand-free $CsPbBr_3$ with calliandra-like nanostructure (LF-CPB CL) can be synthesized easily through a ligand-free seed-assisted dissolution-recrystallization growth process, exhibiting significantly enhanced $CO_2$ uptake capacity. More specifically, the abundant surface bromine (Br) vacancies in ligand-free MHP materials are demonstrated to be beneficial to photogenerated carrier separation. The electron consumption rate of LF-CPB CL for photocatalytic $CO_2$ reduction increases 7 and 20 times over those of traditional ligand-capping $CsPbBr_3$ nanocrystal (L-CPB NC) and bulk $CsPbBr_3$, respectively. Moreover, the absence of ligand hindrance can facilitate the interfacial electronic coupling between LF-CPB CL and tetra(4-carboxyphenyl)porphyrin iron(III) chloride (Fe-TCPP) cocatalyst, bringing forth significantly accelerated interfacial charge separation. The LF-CPB CL/Fe-TCPP exhibits a total electron consumption rate of 145.6 μmol $g^{-1}$ $h^{-1}$ for $CO_2$ photoreduction coupled with water oxidation, which is over 14 times higher than that of L-CPB NC/Fe-TCPP.



## 1. Introduction

Artificial photosynthesis, as a fascinating solution to achieve carbon neutrality, has received ever-increasing scientific attention in the past decade [1,2], which can not only reduce greenhouse gas concentrations but also fundamentally solve the problem of energy, by converting renewable solar energy into solar fuels (i.e., CO, $CH_4$, $CH_3OH$, etc.) with $CO_2$ and $H_2O$ as reactants over catalysts. An ideal artificial photosynthesis catalyst should have a good light-harvesting capacity and high exciton dissociation efficiency, which are also the two main pursuits of most previous studies on photocatalysts [3,4]. Consequently, metal halide perovskites (MHPs) nanocrystals (NCs) have attracted wide attention in the photocatalytic community in the past years [5–8], by virtue of their high light absorption coefficient, long electron-hole diffusion lengths, and tunable bandgaps [9], which have sparked a boom in solar cell, photodetectors, and light-emitting diodes (LEDs) during the last decade [10,11]. For $CO_2$ photoreduction, however, traditional solo-MHPs NCs with long alkyl chain ligands are subject to low-efficiency $CO_2$ uptake capacity and insufficient charge separation efficiency, resulting in very low photocatalytic activity [12].

Benefitting from the previous experience in the construction of traditional semiconductor photocatalysts, the well-known effective strategies such as heterojunction engineering [13,14] and loading cocatalyst [15,16] have also been adopted for constructing halide perovskite-based catalysts to boost photogenerated charge separation [17–20], and the performance of MHPs NCs has been consecutively increased for photocatalytic $CO_2$ reduction [21,22]. Nevertheless, apart from inferior $CO_2$ uptake ability, inefficient interfacial charge transfer is also inevitably restricted by the long-chain organic ligands on the MHPs NCs surface, which seems to have become a sticking point in the design of more efficient artificial photosynthesis catalysts. To solve this problem, the most straightforward strategy is to get rid of the organic ligands on the surface of MHP NCs. While without the protection of surface organic ligands, MHP NCs tend to agglomerate into bulks and cannot maintain the nanoscale configuration needed for efficient

* Corresponding authors.
*E-mail addresses:* zm2016@email.tjut.edu.cn (M. Zhang), lutongbu@tjut.edu.cn (T.-B. Lu).

https://doi.org/10.1016/j.jechem.2022.10.022

photocatalysts, showing an inefficient photocatalytic $CO_2$ reduction activity. Employing the nano-confined space of the templates (such as metal-organic framework [23,24] or metallic oxide [25]) to encapsulate MHP is currently an effective method for preparing ligand-free MHP NCs. Nonetheless, the isolated MHP NCs in these matrixes can not effectively contact the reactants, which will reduce the rate of catalytic reaction. Up to now, it is still challenging to construct ligand-free MHP nanomaterials with a lot of exposed surfaces for artificial photosynthesis.

In this contribution, we reported a facile method to synthesize a series of ligand-free $CsPbBr_3$ nanomaterials with calliandra-like configuration (coded as LF-CPB CLs) through a ligand-free seed-assisted dissolution-recrystallization growth process, and employed them as efficient photocatalysts to drive the overall reaction of $CO_2$ reduction and water oxidation under visible light irradiation. Our strategy to increase the photocatalytic activity is based on the following considerations: (1) The calliandra-like structure consisting of a cluster of nanobelts fixed on the core can prevent the nanobelts from aggregating, thereby improving the stability of LF-CPB CLs. (2) LF-CPB CLs without surfactant capping can expose more surface bromine (Br) vacancies [26], which can improve the $CO_2$ uptake capacity [27]. (3) The surface vacancy defects in MHP materials belong to shallow trap states [28,29], which should ameliorate the exciton dissociation and facilitate photogenerated carriers to participate in redox reaction. (4) Without the hindrance of surface ligands, the charge transfer between LF-CPB CLs and cocatalysts can be greatly accelerated, which contributes to further enhancement of charge separation. As expected, LF-CPB CLs exhibit significantly enhanced photocatalytic performance for $CO_2$ reduction, and the corresponding electron consumption rate is 7 and 20 times higher than those of traditional ligand-capping $CsPbBr_3$ nanocrystals (coded as L-CPB NCs) and LF-CPB bulks, respectively. Moreover, when the common molecular catalyst tetra(4-carboxyphenyl)porphyrin iron(III) chloride (Fe-TCPP) was grafted onto LF-CPB CLs, the photocatalytic activity can be further notably improved. The total electron consumption rate of LF-CPB CLs/Fe-TCPP composite reaches up to 145.6 μmol $g^{-1}$-$h^{-1}$ for $CO_2$ photoreduction integrated with water oxidation, which is almost 14 times over that of the L-CPB NC/Fe-TCPP counterpart.

## 2. Experimental

### 2.1. Sample preparation

Preparation of ligand-capped $CsPbBr_3$ nanocrystals (L-CPB NCs): The traditional L-CPB NCs solid powders were prepared with oleylamine and oleic acid as ligands as described in our previous work [22].

Preparation of ligand-free $CsPbBr_3$ bulks (LF-CPB bulks): The same molar amount of CsBr (21.3 mg) and $PbBr_2$ (36.7 mg) were taken into an agate mortar, and ground for more than 1 h until the reactants completely reacted. The powder was sintered at 350 °C for 2 h, and the obtained powder was ligand-free $CsPbBr_3$ bulks.

Preparation of calliandra-like ligand-free $CsPbBr_3$ (LF-CPB CLs): First, $PbBr_2$ DMF solution (200.0 mg $mL^{-1}$) and $Pb(Ac)_2$ methanol solution (84.0 mg $mL^{-1}$) were prepared respectively. Then, the $PbBr_2$ DMF solution was spin-coated on a 1 $cm^2$ silicon wafer with 3000 r $min^{-1}$ for 30 s. The $PbBr_2$ film was heated at 80 °C for 30 min. After that, 13 mL of $Pb(Ac)_2$ solution was dripped onto $PbBr_2$ film carefully, and then heated at 100 °C for 30 min. Subsequently, the silicon wafer coated with $PbBr_2$ and $Pb(Ac)_2$ was carefully placed in 20.0 mg $mL^{-1}$ CsBr methanol solution (face down, using ultra-dry methanol), and the calliandra-like nanomaterials would spontaneously grow for 16 h. Finally, the sample was washed with methanol for 2 s and then taken out. A series of LF-CPB-*X* CLs (*X* = 1, 2, and 3) can be obtained by changing the concentration of CsBr methanol solution (25.0, 20.0, and 15.0 mg $mL^{-1}$). The catalyst mass can be determined by weighing the mass of the substrate before and after the reaction.

Preparation of LF-CPB CLs/Fe-TCPP composite: 4.0 mg $mL^{-1}$ of Fe-TCPP methanol solution was prepared, and then 30 mL of the above solution was evenly dropped onto the silicon wafer coated with LF-CPB-2 CLs. When the solution was evaporated, LF-CPB-2 CLs/Fe-TCPP composite was obtained.

### 2.2. In-situ irradiated X-ray photoelectron spectroscopy (ISI-XPS)

ISI-XPS measurements were recorded on an ESCALAB250Xi X-ray photoelectron spectrometer. A 300 W Xe-lamp was used as the light source. During the measurement, the light source was set about 40 cm away from the photocatalyst.

### 2.3. In-situ Fourier transforms-infrared spectroscopy (FT-IR)

In-situ FT-IR spectra were obtained on in-situ FT-IR with Bruker TENSOR II equipment using an MCT detector. A 300 W Xe lamp with a UVIRCUT400 filter was used as the light source. During the measurement, $H_2O$ and $D_2O$ were used as reaction substrates, respectively.

### 2.4. Photocatalytic experiments

All the $CO_2$ reduction reactions were performed in a gas-solid reaction apparatus (Fig. S1). 2 mg of the photocatalyst was put in the reaction system. In addition, 100 μL of $H_2O$ was injected into the system as an electron source. The reaction system was degassed to remove $O_2$ and refilled with $CO_2$ and $H_2O$ for 20 min. A 300 W Xe-lamp equipped with a UVIRCUT400 filter was used to simulate the solar irradiation, and the light intensity was adjusted to 100 mW $cm^{-2}$ by calibrating with an NREL-calibrated Si solar cell. 45 h of the photocatalytic experiment was tested to investigate the stability of samples.

### 2.5. Theoretical calculation

Partial density of states (PDOS) for $CsPbBr_3$ was extracted from the electronic band dispersion curves using the Perdue-Burke-Ernzerhof (PBE) of generalized gradient approximation (GGA) function. The cutoff energy was set to 500 eV. During the geometry optimization, the convergence tolerance was set as $1.0 \times 10^{-5}$-eV $atom^{-1}$ for energy.

## 3. Results and discussion

### 3.1. Preparation and structures of LF-CPB CLs

As illustrated in Scheme S1 (Supporting Information), the calliandra-like LF-CPB CLs nanomaterials were prepared through a ligand-free seed-assisted growth strategy, and the details were described in the Methods section. In brief, a thin layer of lead bromide ($PbBr_2$) was initially deposited on a clean silicon wafer by spin coating and evaporating to form a seed layer. Powder X-ray diffraction (PXRD) measurement revealed that the as-prepared seed layer is indexed to orthorhombic phase $PbBr_2$ (Fig. S2). Subsequently, a certain volume of lead acetate ($Pb(Ac)_2$) methanol solution was dispersed on the $PbBr_2$ seed layer drop by drop, and then evaporated to further provide the extra lead source. Finally, the silicon/$PbBr_2$/$Pb(Ac)_2$ was immersed in a cesium bromide (CsBr) methanol solution with top-down standing for 16 h. The LF-CPB

CLs nanomaterials can be obtained via burst nucleation and oriented growth of the CsPbBr3 crystal nucleus. The scanning electron microscopy (SEM) measurements (Fig. 1a–c) confirmed the as-prepared samples with a calliandra-like structure composed of nanobelts.

Upon changing the concentration of CsBr methanol solution (25, 20, and 15 mg $mL^{-1}$), the average widths of the nanobelts can be modulated to 150, 100, and 50 nm (named LF-CPB-1/2/3 CLs). Elemental mapping images of typical LF-CPB-2 CLs (Fig. 1d) verified that Cs, Pb, and Br were distributed evenly on each belt branch of the nanomaterials. The high-resolution transmission electron microscopy (HRTEM) image of LF-CPB-2 CLs (Fig. 1e) identified the lattice spacing of 0.41 nm, corresponding to the (200) plane of orthorhombic phase $CsPbBr_3$. The X-ray diffraction (XRD) results (Fig. 1f) indicated that the $PbBr_2$ substrates were completely transformed to $CsPbBr_3$, exhibiting high crystallinity with strong diffraction peaks of orthorhombic $CsPbBr_3$ (JCPDS card No. 01-072-7929). The peaks at 15.4°, 15.6°, 21.9°, 22.0°, 30.7°, and 31.1° can be corresponding to the (002), (110), (112), (200), (004), and (220) facets of orthorhombic $CsPbBr_3$, respectively. As the width of nanobelts in LF-CPB CLs decreases, the strength ratio of (112)/(220) increases from 1.04 to 1.67, which is related to the anisotropic growth of the nanobelts [30].

To reveal the formation mechanism of the LF-CPB CLs, some controlled experiments were performed under different reaction conditions. Firstly, we stopped the reaction at different growth stages and monitored the morphology evolution of LF-CPB CLs to speculate on the growth process (Fig. S3). In the initial stage (stop the reaction time at 3 min), nanoparticle-assembled clusters with an average overall size of 50 nm were observed (Fig. S3a). The XRD results confirmed that the obtained clusters are orthorhombic $CsPbBr_3$ (Fig. S3d). Considering the high concentration of CsBr and its fast reaction rate with halide and lead ions, burst nucleation probably occurred as the silicon wafer coated with $PbBr_2$ and $Pb(Ac)_2$ was immersed in CsBr methanol solution owing to the high solubility of $Pb(AC)_2$ in methanol solvent. Meanwhile, the initial crystal nucleuses tended to grow and aggregate into nanoparticle-assembled clusters for reducing surface energy. Then the nanoparticles would grow outward into nanobelts via a dissolution and recrystallization process from the silicon surface (Fig. S3b) due to the thermodynamically favorable generation of $PbBr_4^{2-}$ species at the solid-liquid interface, which has been demonstrated to occur easily in the presence of high concentration $Br^-$ following the reaction $CsPbBr_3(s) + Br^-(l) \rightarrow Cs^+(l) + PbBr_4^{2-}(l)$ [31]. Subsequently, the local oversaturated $PbBr_4^{2-}$ at the solid-liquid interface in the CsBr solution will in turn react with $Cs^+$ through slow recrystallization to grow into the calliandra-like configuration consisting of $CsPbBr_3$ nanobelts (Fig. S3c). The influence of $Pb(Ac)_2$ concentration on the morphology of the $CsPbBr_3$ nanostructure in the initial and final stages was further investigated (see details in Supporting Information Figs. S4 and S5 and corresponding notes), which revealed that the growth of LF-CPB CLs probably undergoes the formation of nanoparticle-assembled clusters via burst nucleation and following 1D growing through dissolution and recrystallization process as shown in Fig. S6. During the $CsPbBr_3$ growth, the concentration of the CsBr precursor needs to be high for allowing burst nucleation and the transformation of the Pb source into $CsPbBr_3$ via a dissolution and recrystallization process. $CsPbBr_3$ without burst nucleation would grow into bulk particles (Fig. S7). Meanwhile, a proper amount of soluble Pb source is required for providing sufficient nuclei to form nanoparticle-assembled clusters.

### 3.2. Thermodynamic and $CO_2$ uptake properties

The energy band structures of LF-CPB CLs were assessed by measuring their UV-Vis diffuse reflectance spectra (DRS) and ultraviolet photoelectron spectra (UPS). As a reference, the L-CPB NCs with end-capping ligands were also evaluated under identical conditions. As displayed in Fig. 2(a), the results of Tauc plots derived from UV-Vis DRS (Fig. S8) confirm that the bandgaps of as-prepared LF-CPB-*X* CLs (*X* = 1, 2, and 3) and L-CPB NCs are 2.25, 2.27, 2.28, and 2.30 eV, respectively. With the decrease of nanobelt width in LF-CPB CLs, the absorption edge has a trend of blue shift owing to the size effect. Meanwhile, at the band tail, the LF-CPB CLs have an absorption expansion relative to L-CPB NCs, due to the scattering of the incident light by the nanobelts in LF-CPB CLs, which is conducive to improving photon capture [32]. According to the results of UPS (Fig. 2b), the valence band edge (VB) position of L-CPB NCs is located at 1.26 V vs. the normal hydrogen electrode (NHE). For all LF-CPB CLs, the VB position is more positive than that of L-CPB NCs. This may be due to the absence of ligand passivation on the surface of LF-CPB CLs, leading to the increase of surface defects, and further changing the electronic structure of nanomaterials [33,34]. The VB values of LF-CPB CLs become more positive along with the shrinkage of size from 1.33 to

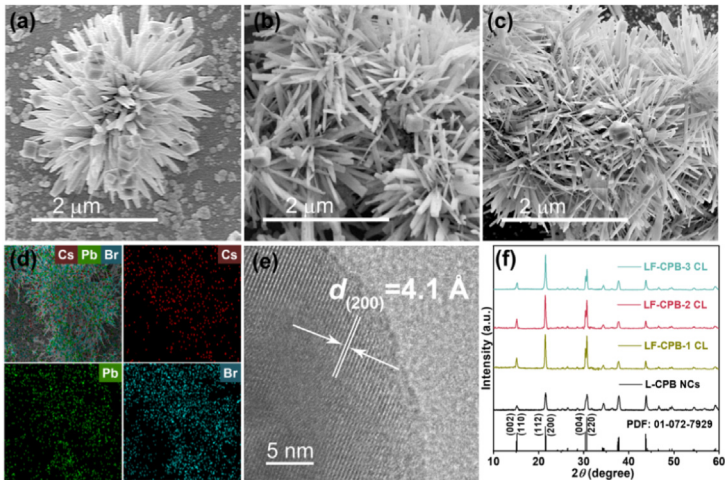


**Fig. 1.** (a–c) SEM images of LF-CPB-*X* CLs (*X* = 1, 2, and 3). (d) The energy-dispersive X-ray spectroscopy (EDS) mapping images of LF-CPB-2 CLs. (e) HR-TEM image of LF-CPB-2 CLs. (f) XRD patterns of L-CPB NCs and LF-CPB-*X* CLs (*X* = 1, 2, and 3).

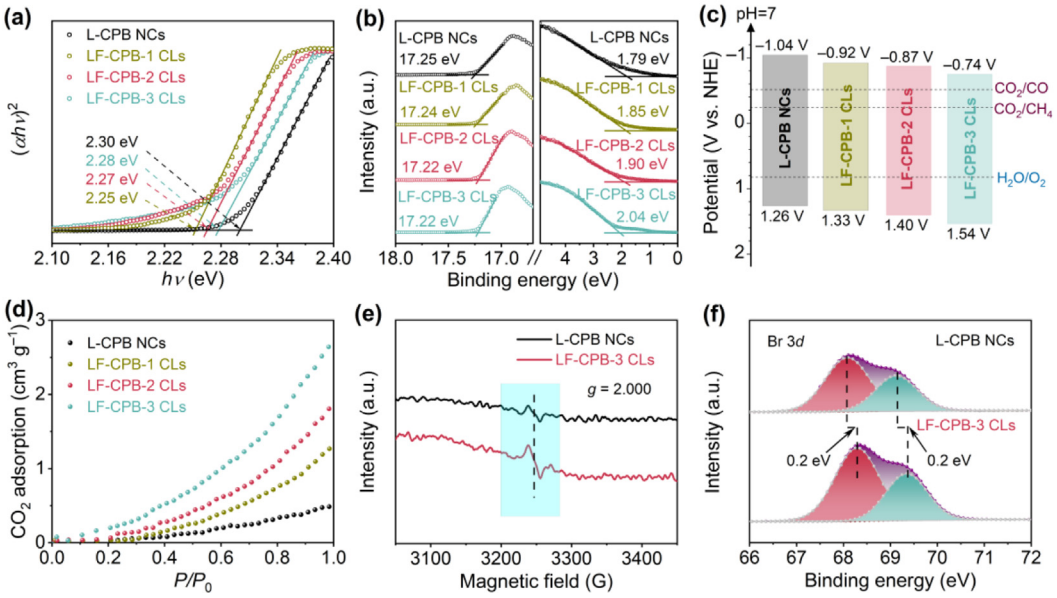


**Fig. 2.** (a) Tauc plots derived from UV-vis DRS spectra, (b) UPS spectra, (c) Band structure diagrams, and (d) $CO_2$ adsorption curves of L-CPB NCs and LF-CPB-*X* CLs (*X* = 1, 2, and 3). (e) ESR spectra of L-CPB NCs and LF-CPB-3 CLs. (f) High-resolution XPS spectra for Br 3*d* in L-CPB NCs and LF-CPB-3 CLs.

1.54 V (vs. NHE). The positive shift of the VB will increase the thermodynamic driving force of water oxidation, which is beneficial to improving the overall catalytic activity. The conduction band edge (CB) position can be deduced from the results of bandgap and VB, and the detailed parameters are presented in Fig. 2(c). It can be seen that the energy band structures of all samples are in the appropriate thermodynamic position to drive overall artificial photosynthesis.

It is widely recognized that high $CO_2$ concentration around the photocatalytic active center is beneficial to improving photocatalytic performance [35]. Therefore, we further performed the $CO_2$ adsorption measurements to evaluate the $CO_2$ uptake capacities of LF-CPB CLs and L-CPB NCs. As shown in Fig. 2(d), the $CO_2$ adsorption capacities of all LF-CPB CLs are much better than that of L-CPB NCs, and become stronger with the decrease of nanobelt size owing to the increase of specific surface area. The significantly enhanced $CO_2$ uptake capacity of LF-CPB CLs should be mainly attributed to the absence of surface ligand passivation, which not only facilitates the proximity of $CO_2$ to the surface of LF-CPB CLs but also provides abundant defect sites for $CO_2$ adsorption. The electron spin resonance (ESR) spectrum measurements were further carried out to uncover the type of defects. As shown in Fig. 2(e), an obvious signal located at $g$ = 2.000 can be observed for both L-CPB NCs and LF-CPB CLs, which could be assigned to the Br vacancy signal [36]. Compared with the L-CPB NCs, LF-CPB-3 CLs exhibits an enhanced ESR signal, implying a higher concentration of Br vacancies existed on LF-CPB-3 CLs. This inference can be further confirmed by monitoring their X-ray photoelectron spectrum (XPS) characteristics. As shown in Fig. 2(f), the Br 3*d* peak of LF-CPB-3 CLs has a 0.25 eV upshift relative to L-CPB NCs, and there is a downshift of the Pb 4*f* XPS peak for the LF-CPB-3 CLs in comparison with L-CPB NCs (Fig. S9), further verifying the existence of higher concentration of Br vacancies in LF-CPB-3 CLs [37]. Moreover, by analyzing the XPS data, the Pb/Br ratios in LF-CPB-*X* CLs (*X* = 1, 2, and 3) have been determined, to be 1/2.94, 1/2.81, and 1/2.72 respectively, suggesting that these catalysts present a lead-rich surface. The surface Br vacancy defects in MHP materials have been demonstrated to be capable of forming surface shallow trap states [38], which could effectively trap photogenerated electrons and suppress electron-hole recombination.

### 3.3. Photogenerated carrier dynamics

The evolution process of photogenerated carriers was investigated by recording the fluorescence lifetime micrographs of L-CPB NCs and LF-CPB CLs (Fig. 3a–d) with the aid of a time-resolved confocal fluorescence microscope. The intensity of the light and shade in the images represent the intensity change of the steady-state photoluminescence (PL) intensity, and the gradual change of the color represents the evolution of the PL lifetime for different samples. The corresponding statistical analysis results are summarized in Fig. 3(e). Specifically, LF-CPB CLs have obvious PL quenching and lifetime decay compared with L-CPB NCs, which was mainly due to the abundant Br vacancies of LF-CPB CLs that provide more charge transfer channels for photogenerated electrons [26]. The gradually intensified quenching and decay from LF-CPB-1 CLs to LF-CPB-3 CLs are due to the increase of Br vacancies concentration. The Br vacancy-related PL quenching can be further confirmed by measuring the transient PL decay curves of L-CPB NCs and LF-CPB CLs as depicted in Fig. 3(f), which exhibits an accelerated PL decay with increasing Br vacancy concentration, and the corresponding multiexponential fitting parameters are compiled in Table S1. The short-time component ($\tau_1$) and the long-time component ($\tau_2$) are related to the photogenerated charge transfer and recombination of photogenerated carriers in $CsPbBr_3$, respectively. The proportion of $\tau_1$ is gradually increasing from L-CPB NCs to LF-CPB-3 CLs, while the proportion of $\tau_2$ is gradually decreasing (Table S1). These results indicate that the Br vacancies can promote the separation of carriers and inhibit the recombination of electron-hole pairs, which can improve the utilization efficiency of photogenerated carriers for photocatalytic reactions.

To further confirm the benefit of the Br vacancy defect for photogenerated carrier separation, we also monitored the photogenerated carrier deactivation kinetics with nanosecond laser flash photolysis equipment. The nanosecond transient absorption (ns-TA) spectra of L-CPB NCs and LF-CPB CLs (Fig. 4a–d) show that an obvious negative signal can be observed near 520 nm after exciting with a 410 nm pulsed laser for all the samples, owing to the ground-state bleaching (GSB) of $CsPbBr_3$. Additionally, a clear red shift for the GSB signal of LF-CPB CLs can be observed compared

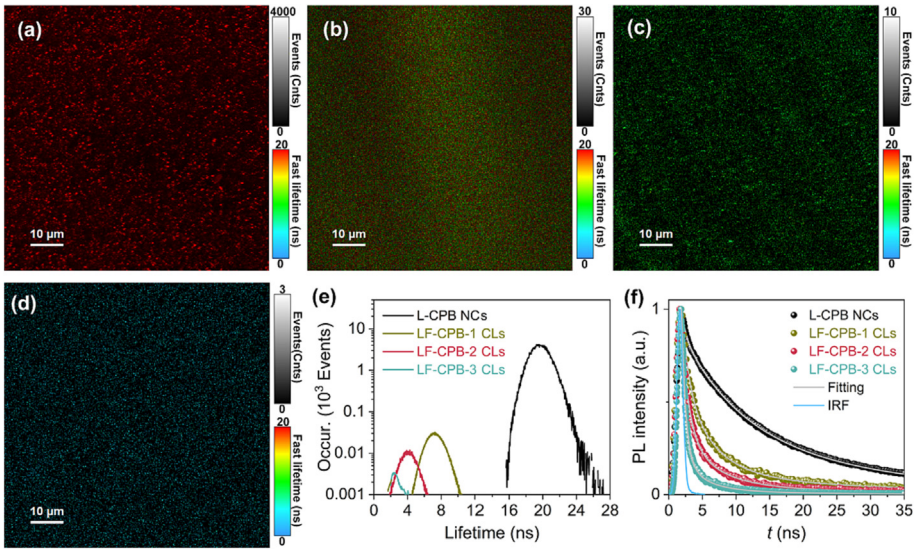


**Fig. 3.** Fluorescence lifetime imaging microscopy (FLIM) images of (a) L-CPB NCs and (b–d) LF-CPB-*X* CLs (*X* = 1, 2, and 3), and (e) the corresponding statistical analysis of the FLIM over the entire image (Fig. 3a–d). (f) PL decay traces of L-CPB NCs and LF-CPB-*X* CLs (*X* = 1, 2, and 3).

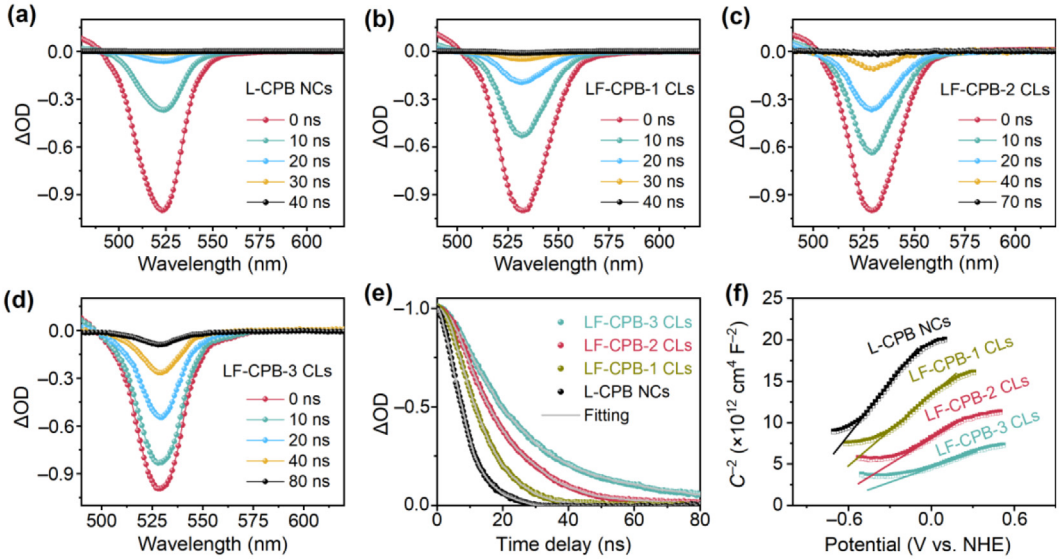


**Fig. 4.** Nanosecond transient absorption (ns-TA) spectroscopy at indicated delay times after 410 nm optical excitation of (a) L-CPB NCs and (b–d) LF-CPB-*X* CLs (*X* = 1, 2, and 3), and (e) ns-TA kinetic plots of L-CPB NCs and LF-CPB-*X* CLs (*X* = 1, 2 and 3) monitored at respective GSB peak. (f) Mott-Schottky plots under light irradiation for L-CPB NCs and LF-CPB-X CLs (*X* = 1, 2, and 3).

with that of L-CPB NCs, similar to the changing trend in steady-state absorption (Fig. S8). This should be mainly due to the formation of the band-like structure of the surface trap energy level and other energy levels in the bandgap of $CsPbBr_3$ [39]. In general, the appearance of GSB under light illumination originated from the increase in the number of excited-state particles relative to the number of ground-state particles, and its recovery process is related to carrier recombination or removal [40]. According to the ns-TA kinetics plots (Fig. 4e) at GSB peaks, all the LF-CPB CLs have longer GSB recovery times than L-CPB NCs, and the recovery process gradually slows down as the decrease of nanobelt width for LF-CPB CLs (from LF-CPB-1 CLs to LF-CPB-3 CLs). This phenomenon implies that the formation of shallow trap states generated by surface Br vacancy defects can provide convenient pathways to capture photogenerated electrons, resulting in the delayed recombination of photogenerated carriers. That is, the excited electrons have more chances to transfer to the surface of LF-CPB CLs, which can more effectively promote the photocatalytic reaction.

Furthermore, the nonequilibrium carrier concentrations of samples were calculated by the Mott-Schottky curve. Normally, the smaller the tangent slope of the Mott-Schottky curve, the higher the carrier concentration. A higher concentration of nonequilibrium carriers involved in redox reactions is beneficial for the improvement of photocatalytic activity [41]. As can be seen in Fig. 4(f), there is a gradual decrease in the slope of the curve from L-CPB NCs to LF-CPB-3 CLs, indicating a higher nonequilibrium carrier concentration in LF-CPB-3 CLs. This result is consistent with the information obtained from the ns-TA spectra, further demonstrating more efficient photogenerated carrier separation characteristics for LF-CPB CLs with respect to L-CPB NCs. The specific carrier concentration values of samples were calculated with equa-

tions a and b in Table S2 [9,42]. It can be seen more intuitively that the carrier concentration of LF-CPB-3 CLs ($9.25 \times 10^{17}$ $cm^{-3}$) is much higher than those of L-CPB NCs ($2.77 \times 10^{17}$ $cm^{-3}$) and other LF-CPB CLs (LF-CPB-1 CLs: $4.07 \times 10^{17}$ $cm^{-3}$; LF-CPB-2 CLs: $6.61 \times 10^{17}$ $cm^{-3}$).

In addition, electrochemical analyses were also performed to investigate the photogenerated carrier separation through photocurrent response (*I-t*) and electrochemical impedance spectroscopy (EIS) measurements. As depicted in Fig. S10, LF-CPB-3 CLs exhibit the highest photocurrent density among the evaluated samples, and the photocurrent density gradually decreases from LF-CPB-3 CLs to L-CPB NCs, which are consistent with the results of the above transient PL and ns-TA spectra measurements. In addition, EIS measurements (Fig. S11a) revealed that the charge transport resistances of LF-CPB-1 CLs, LF-CPB-2 CLs, and LF-CPB-3 CLs are 4851, 2995, 2273 Ω, respectively, which are distinctly smaller than that (8826 Ω) of L-CPB NCs (Table S3). The accelerated charge transport induced by the increase in Br vacancy defects further confirms the benefit of Br vacancy defects for charge separation. The bode phase diagrams (Fig. S11b) derived from the impedance spectroscopies further verified that the LF-CPB CLs have a longer free-carrier lifetime with respect to nanocrystals with ligand capping (Table S3), which is more conducive for carriers to participate in the surface redox reaction of $CsPbBr_3$.

### 3.4. Interfacial interaction and charge transfer between LF-CPB and Fe-TCPP

Apart from the ameliorative photogenerated carrier separation, the absence of ligands should also benefit the loading of cocatalysts on the MHP surface, which is usually a common strategy to improve photocatalytic activity. Herein, Fe-TCPP as a traditional molecular cocatalyst was selected to graft on the LF-CPB CLs. Considering the energy level matching (Fig. S12 and Fig. 2c), LF-CPB-2 CLs were chosen as the research object to form the LF-CPB-2 CLs/Fe-TCPP composite photocatalyst (see Experimental section for preparation details). The EDS mapping images (Fig. S13) confirmed the homogeneous distribution of Fe-TCPP on LF-CPB-2 CLs. Moreover, high-resolution XPS measurements (Fig. 5) revealed that there is a significant shift of binding energy for Cs 3*d*, Pb 4*f*, Br 3*d*, and O 1*s* (by 0.6 eV) in LF-CPB-2 CLs/Fe-TCPP with respect to individual LF-CPB-2 CLs and Fe-TCPP, demonstrating a strong electronic coupling between LF-CPB CLs and Fe-TCPP. On the contrary, only a small binding energy shift (by 0.2 eV) occurred (Fig. S14) in L-CPB NCs/Fe-TCPP compared with pristine L-CPB NCs and Fe-TCPP, respectively, indicating that the interfacial bonding between L-CPB NCs and Fe-TCPP was inhibited by the surface ligands of L-CPB NCs. These results demonstrate that the ligand-free growth method can effectively ensure the interface connection between LF-CPB CLs and cocatalyst, and then promote the interface charge transfer of the composite, which should be conducive to the improvement of photocatalytic activity.

The interfacial charge transfer kinetics of L-CPB NCs/Fe-TCPP and LF-CPB-2 CLs/Fe-TCPP were further investigated by time-resolved confocal fluorescence microscopy and transient PL spectra. As presented in Figs. S15 and S16(a), more obvious PL quenching and decay were observed for LF-CPB-2 CLs/Fe-TCPP than L-CPB NCs/Fe-TCPP, which firmly proved the advantage of LF-CPB CLs in interfacial charge transfer. According to the transient PL decay curves (Fig. S16b), the PL decay efficiencies ($\eta_{decay}$) can be calculated to be 14% and 78% (Table S4) for L-CPB NCs/Fe-TCPP and LF-CPB-2 CLs/Fe-TCPP, respectively, demonstrating the unique advantage in advantage achieving efficient interfacial charge transfer and separation for the LF-CPB CLs based on ligand-free growth strategy compared with traditional ligand-capped $CsPbBr_3$ NCs. In addition, according to the in-situ irradiated-XPS (ISI-XPS) measurements, the characteristic peaks of Fe 2*p* XPS in LF-CPB-2 CLs/Fe-TCPP shifted to the lower energy direction after illumination (Fig. S17), indicating that Fe can accept photogenerated electrons and serve as the catalytic site for photocatalytic $CO_2$ reduction.

### 3.5. Photocatalytic $CO_2$ reduction coupled with water oxidation

The photocatalytic $CO_2$ reduction activities of these halide perovskite-based samples were evaluated in a gas-solid reaction apparatus filled with $CO_2$ and $H_2O$ vapor (Fig. S1). For LF-CPB bulks,

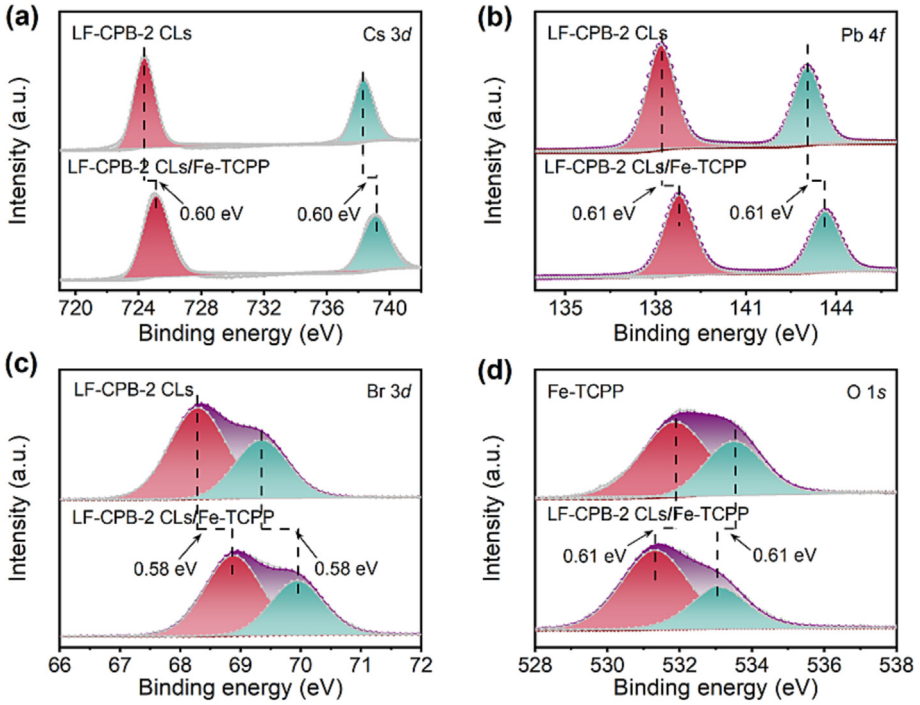


**Fig. 5.** High-resolution XPS of LF-CPB-2 CLs, Fe-TCPP and LF-CPB-2 CLs/Fe-TCPP composite: (a) Cs 3*d*, (b) Pb 4*f*, (c) Br 3*d* and (d) O 1*s*.

L-CPB NCs, and LF-CPB-X CLs ($X$ = 1, 2, and 3), gas chromatographic analysis results revealed that $CH_4$ and CO were the main reduction products, with negligible $H_2$ (Fig. S18), which has been commonly observed in other photocatalytic systems based on halide perovskites [18–20]. The electron consumption rate of LF-CPB-3 CLs can reach 49 μmol $g^{-1}$ $h^{-1}$, which is much higher than those of L-CPB NCs (6.8 μmol $g^{-1}$ $h^{-1}$) and LF-CPB bulks (2.4 μmol $g^{-1}$ $h^{-1}$) (Fig. 6a). This is attributed to the abundant Br vacancy defects on the surface of LF-CPB CLs, which can enhance $CO_2$ uptake capacity and accelerate photogenerated carrier separation. In addition, the catalytic activity increases with decreasing the width of nanobelts in LF-CPB CLs, which should be attributed to the increase of surface Br vacancy defects and the enhancement of the driving force for water oxidation (Fig. 2c) with decreasing nanobelt size. Moreover, both LF-CPB CLs and L-CPB NCs exhibit better catalytic activity than LF-CPB bulks, owing to the well-known unique advantages of nanomaterials in photocatalytic reactions.

Furthermore, grafting Fe-TCPP on the surface of LF-CPB-2 CLs can significantly enhance the photoreduction $CO_2$ activity, and the electron consumption rate was increased by nearly 5 times, reaching 145.6 μmol $g^{-1}$ $h^{-1}$ (Fig. 6b). In contrast, the photocatalytic activity of L-CPB NCs/Fe-TCPP is only slightly improved compared with pristine L-CPB NCs from 6.8 to 10.8 μmol $g^{-1}$ $h^{-1}$. This phenomenon is consistent with the results of XPS (Fig. 5 and Fig. S14) and transient spectrum measurements (Fig. S16), which is mainly due to the formation of strong interface electron coupling between LF-CPB-2 CLs and Fe-TCPP, thus forming a convenient interface charge transfer channel. The resultant efficient charge separation can ultimately boost the improvement of photocatalytic activity. In addition, the long-term photocatalytic tests indicated good stability for LF-CPB-2 CLs/Fe-TCPP in the gas-solid reaction system, compared with L-CPB NCs (Fig. 6c and Fig. S19). Ligand-terminated nanocrystals (L-CPB NCs) could agglomerate due to ligand decomposition in the photocatalytic process, which reduces the photocatalytic activity, while LF-CPB CLs maintained their intrinsic catalytic activity. Meanwhile, it can be seen that there are no changes in XRD patterns, SEM image, and XPS (Figs. S20–S22) for LF-CPB-2 CLs/Fe-TCPP before and after photocatalytic reaction, further proving the stability of LF-CPB-2 CLs/Fe-TCPP in the gas-solid reaction system.

Considering that the valence band maximum of $CsPbBr_3$ is mainly contributed by the antibonding interaction between the Br 4*p* and the Pb 6*s* orbitals, while the conduction band minimum mainly arises from the Pb 6*p* orbital (Fig. 6d and e) [43], the active site of pristine $CsPbBr_3$ for photocatalytic $CO_2$ reduction should be the unsaturated bonded Pb site. The Br vacancy constructed on LF-CPB CLs effectively exposes the Pb site, which greatly improves the photocatalytic activity. According to the previously suggested reaction path of the perovskite-based catalysts for photocatalytic $CO_2$ to CO and $CH_4$ [44,45], the following processes mainly occur during the $CO_2$ photoreduction process ($CO_2 + 2e^- + 2H^+ \rightarrow CO + H_2O$; $CO_2 + 8e^- + 8H^+ \rightarrow CH_4 + 2H_2O$): firstly, the adsorbed $CO_2$ on Pb (for pristine $CsPbBr_3$) or Fe (when adding Fe-TCPP cocatalyst) site is activated to generate $CO_2^*$ species; Then, the COOH* species is generated after $CO_2^*$ species protonation; Finally, the COOH* species is successively protonated and dehydrated to generate CO*, which can desorb from the photocatalyst to generate CO product. Meanwhile, if CO* species further undergo multi-step protonated and dehydrated processes, the $CH_4$ product was generated [46].

In addition, using LF-CPB-2 CLs/Fe-TCPP as a photocatalyst, nearly stoichiometric $O_2$ (35.5 μmol $g^{-1}$ $h^{-1}$) can be obtained as an oxidation product, demonstrating an effective utilization for the photogenerated holes (Fig. 6c) through the water oxidation reaction: $2H_2O + 4\ h^+ \rightarrow O_2 + 4H^+$. Furthermore, the mechanism of photocatalytic water oxidation using halide perovskite was explored by in-situ Fourier transform-infrared spectroscopy (FT-IR). As shown in Fig. 6(f), when $H_2O$ and $D_2O$ were used as solvents respectively, an absorption peak appeared at 830 and 800 $cm^{-1}$ under light, which can be attributed to the O—O single bond stretch of a peroxide moiety [47]. Considering that the D isotope can redshift the infrared characteristic signal due to the coupling of OH (OD) bending mode with the OO stretch, so the observed sig-

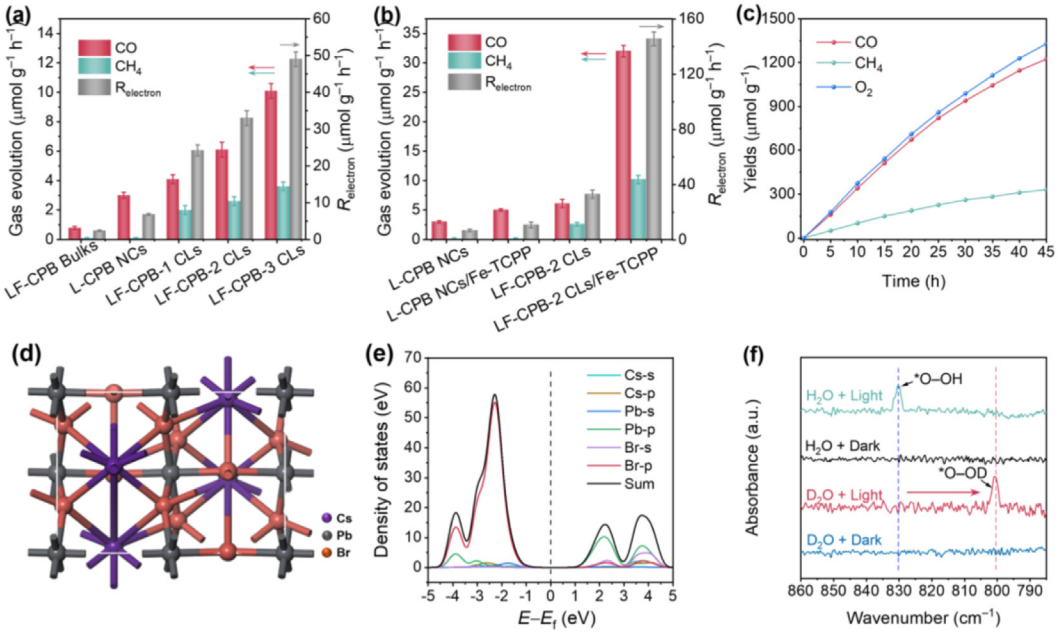


**Fig. 6.** (a and b) The gas generation rate and corresponding electron reduction rate ($R_{electron}$) of LF-CPB bulks, L-CPB NCs, LF-CPB-$X$ CLs ($X$ = 1, 2, and 3), L-CPB NCs/Fe-TCPP, and LF-CPB-2 CLs/Fe-TCPP. $R_{CO}$ and $R_{CH4}$ denote the electron reduction rates of $CO_2$ to CO and $CO_2$ to $CH_4$, respectively, $R_{electron} = 2R_{CO} + 8R_{CH4}$. (c) The long-term photocatalytic $CO_2$ reduction testing with LF-CPB-2 CLs/Fe-TCPP as the photocatalyst. Reaction condition: 300 W Xe-lamp with UVIRCUT400 filter with the light intensity of 100 mW $cm^{-2}$. (d) Lattice structure and (e) partial density of states (PDOS) for $CsPbBr_3$ extracted from the electronic band dispersion curves. (f) In-situ FT-IR of $H_2O$ (and $D_2O$) oxidation intermediates on as-prepared LF-CPB-2 CLs/Fe-TCPP composite under light and dark conditions.

nal at 830 and 800 $cm^{-1}$ can be identified as a hydroperoxide (*O–OH and *O–OD) species. The formation of the O–O bond in halide perovskite water oxidation can be identified as a water nucleophilic attack (WNA) mechanism, that is, an electrophilic *O and a nucleophilic water molecule reacted on a single catalytic site [48].

Finally, some control experiments were further performed with LF-CPB-2 CLs/Fe-TCPP as a photocatalyst to disclose the origin of products (Fig. S23): (1) photocatalyst + $CO_2$ + $H_2O$; (2) photocatalyst + Ar + $H_2O$; (3) photocatalyst + $CO_2$; (4) without photocatalyst + $CO_2$ + $H_2O$. According to the results of gas chromatography analyses, only condition one had gas product formation, which implied that the photocatalytic reaction was based on the conversion of $CO_2$ and $H_2O$ feedstocks to CO, $CH_4$, and $O_2$. In addition, the isotopically labeled $^{13}CO_2$ experiment was performed under the same conditions, where obvious $^{13}CO$ ($m/z$ = 29) and $^{13}CH_4$ ($m/z$ = 17) signals can be identified in MS analysis (Fig. S24). Meanwhile, $^{18}O_2$ can be detected with the isotopically labeled $H_2^{18}O$ as feedstocks (Fig. S25). These results can confirm that the detected CO and $CH_4$ products originated from $CO_2$ photoreduction, and $O_2$ was derived from $H_2O$ oxidation.

## 4. Conclusions

To summarize, we have demonstrated the facile synthesis of ligand-free $CsPbBr_3$ with calliandra-like nanostructure via a ligand-free seed-assisted growth strategy through a dissolution-recrystallization growth process, and employed them as efficient photocatalysts for $CO_2$ reduction coupled with water oxidation. This crystal growth strategy endows LF-CPB CLs with abundant surface Br vacancy defects, and these surface shallow traps can capture photogenerated electrons to enhance carrier separation as demonstrated by photophysical and electrophysical measurements, bringing forth a significant improvement in the catalytic activity of $CO_2$ photoreduction. It should be noted that $CsPbBr_3$ can directly contact cocatalysts to form a strong interfacial electron coupling and promote efficient interfacial charge transfer, due to the removed hindrance of long-chain alkyl organic ligands on the surface, which are desirable for the construction of efficient composite photocatalysts. This work has not only enriched the nanostructures of the MHP family but also provided a facile strategy for improving the activity of $CO_2$ photoreduction by employing the surface halide defects of MHP. Moreover, the controlled construction of ligand-free MHP nanomaterials will offer an opportunity for developing MHP-based composites with efficient photogenerated carrier separation, promoting their application in artificial photosynthesis and other solar-to-fuel conversion fields.

## Declaration of competing interest

The authors declare that they have no known competing financial interests or personal relationships that could have appeared to influence the work reported in this paper.

## Acknowledgments

This work was financially supported by the Natural Science Foundation of Tianjin City (17JCJQJC43800), the National Key R&D Program of China (2017YFA0700104), the National Science Foundation of China (21931007, U21A20286), Jiangsu Funding Program for Excellent Postdoctoral Talent and the 111 Project of China (D17003).

## Appendix A. Supplementary data

Supplementary data to this article can be found online at https://doi.org/10.1016/j.jechem.2022.10.022.

## References

[1] O.S. Bushuyev, P. De Luna, C.T. Dinh, L. Tao, G. Saur, J. van de Lagemaat, S.O. Kelley, E.H. Sargent, Joule 2 (2018) 825–832.
[2] B. Zhang, L. Sun, Chem. Soc. Rev. 48 (2019) 2216–2264.
[3] H. Wang, H. Zhang, J. Wang, Y. Gao, F. Fan, K. Wu, X. Zong, C. Li, Angew. Chem. Int. Ed. 60 (2021) 7376–7381.
[4] C. Huang, J. Qiao, R.-N. Ci, X.-Z. Wang, Y. Wang, J.-H. Wang, B. Chen, C.-H. Tung, L.-Z. Wu, Chem 7 (2021) 1244–1257.
[5] S. Park, W.J. Chang, C.W. Lee, S. Park, H.-Y. Ahn, K.T. Nam, Nat. Energy 2 (2016) 16185.
[6] J. Hou, S. Cao, Y. Wu, Z. Gao, F. Liang, Y. Sun, Z. Lin, L. Sun, Chem. Eur. J. 23 (2017) 9481–9485.
[7] X. Zhu, Y. Lin, Y. Sun, M.C. Beard, Y. Yan, J. Am. Chem Soc. 141 (2019) 733–738.
[8] P. Zhou, H. Chen, Y. Chao, Q. Zhang, W. Zhang, F. Lv, L. Gu, Q. Zhao, N. Wang, J. Wang, S. Guo, Nat. Commun. 12 (2021) 4412.
[9] G. Xing, N. Mathews, S. Sun, S.S. Lim, Y.M. Lam, M. Grätzel, S. Mhaisalkar, T.C. Sum, Science 342 (2013) 344–347.
[10] R. Yang, R. Li, Y. Cao, Y. Wei, Y. Miao, W.L. Tan, X. Jiao, H. Chen, L. Zhang, Q. Chen, H. Zhang, W. Zou, Y. Wang, M. Yang, C. Yi, N. Wang, F. Gao, C.R. McNeill, T. Qin, J. Wang, W. Huang, Adv. Mater. 30 (2018) 1804771.
[11] X.-K. Liu, W. Xu, S. Bai, Y. Jin, J. Wang, R.H. Friend, F. Gao, Nat. Mater. 20 (2021) 10–21.
[12] Y. Xu, W. Zhang, K. Su, Y.-X. Feng, Y.-F. Mu, M. Zhang, T.-B. Lu, Chem. Eur. J. 27 (2021) 2305–2309.
[13] M. Zhang, M. Lu, Z.-L. Lang, J. Liu, M. Liu, J.-N. Chang, L.-Y. Li, L.-J. Shang, M. Wang, S.-L. Li, Y.-Q. Lan, Angew. Chem. Int. Ed. 59 (2020) 6500–6506.
[14] J. Dong, Y. Kong, H. Cao, Z. Wang, Z. Zhang, L. Zhang, S. Sun, C. Gao, X. Zhu, J. Bao, J. Energy Chem. 64 (2022) 103–112.
[15] J. Ran, M. Jaroniec, S.-Z. Qiao, Adv. Mater. 30 (2018) 1704649.
[16] H. Zhang, Y. Wang, S. Zuo, W. Zhou, J. Zhang, X.W.D. Lou, J. Am. Chem. Soc. 143 (2021) 2173–2177.
[17] Y.-F. Xu, M.-Z. Yang, B.-X. Chen, X.-D. Wang, H.-Y. Chen, D.-B. Kuang, C.-Y. Su, J. Am. Chem. Soc. 139 (2017) 5660–5663.
[18] M. Ou, W. Tu, S. Yin, W. Xing, S. Wu, H. Wang, S. Wan, Q. Zhong, R. Xu, Angew. Chem. Int. Ed. 57 (2018) 13570–13574.
[19] Z. Chen, Y. Hu, J. Wang, Q. Shen, Y. Zhang, C. Ding, Y. Bai, G. Jiang, Z. Li, N. Gaponik, Chem. Mater. 32 (2020) 1517–1525.
[20] F. Xu, K. Meng, B. Cheng, S. Wang, J. Xu, J. Yu, Nat. Commun. 11 (2020) 4613.
[21] J. Wang, J. Liu, Z. Du, Z. Li, J. Energy Chem. 54 (2021) 770–785.
[22] Y.-F. Mu, W. Zhang, G.-X. Dong, K. Su, M. Zhang, T.-L. Lu, Small 16 (2020) 2002140.
[23] L.-Y. Wu, Y.-F. Mu, X.-X. Guo, W. Zhang, Z.-M. Zhang, M. Zhang, T.-B. Lu, Angew. Chem. Int. Ed. 58 (2019) 9491–9495.
[24] F.-Y. Qiao, D. Guan, S. Yuan, H. Rao, X. Chen, J.-A. Wang, J.-S. Qin, J.-J. Xu, J. Yu, J. Am. Chem. Soc. 143 (2021) 14253–14260.
[25] Y. Wei, Z. Cheng, J. Lin, Chem. Soc. Rev. 48 (2019) 310–350.
[26] D. Yang, X. Li, W. Zhou, S. Zhang, C. Meng, Y. Wu, Y. Wang, H. Zeng, Adv. Mater. 31 (2019) 1900767.
[27] P. Chen, Y. Huang, Z. Shi, X. Chen, N. Li, Materials 14 (2021) 2469.
[28] D.P. Nenon, K. Pressler, J. Kang, B.A. Koscher, J.H. Olshansky, W.T. Osowiecki, M. A. Koc, L.-W. Wang, A.P. Alivisatos, J. Am. Chem. Soc. 140 (2018) 17760–17772.
[29] J. Pan, X. Li, X. Gong, J. Yin, D. Zhou, L. Sinatra, R. Huang, J. Liu, J. Chen, I. Dursun, A.M. El-Zohry, M.I. Saidaminov, H.-T. Sun, O.F. Mohammed, C. Ye, E.H. Sargent, O.M. Bakr, Angew. Chem. Int. Ed. 58 (2019) 16077–16081.
[30] C. Zhang, J. Chen, S. Wang, L. Kong, S.W. Lewis, X. Yang, A.L. Rogach, G. Jia, Adv. Mater. 32 (2020) 2002736.
[31] Y. Fu, F. Meng, M.B. Rowley, B.J. Thompson, M.J. Shearer, D. Ma, R.J. Hamers, J.C. Wright, S. Jin, J. Am. Chem. Soc. 137 (2015) 5810–5818.
[32] H. Huang, T. Zhang, X. Cai, Z. Guo, S. Fan, Y. Zhang, C. Lin, T. Gan, H. Hu, Z. Huang, ACS Appl. Mater. Interfaces 13 (2021) 60337–60350.
[33] Y. Cao, N. Wang, H. Tian, J. Guo, Y. Wei, H. Chen, Y. Miao, W. Zou, K. Pan, Y. He, H. Cao, Y. Ke, M. Xu, Y. Wang, M. Yang, K. Du, Z. Fu, D. Kong, D. Dai, Y. Jin, G. Li, H. Li, Q. Peng, J. Wang, W. Huang, Nature 562 (2018) 249–253.
[34] Q. Ruan, T. Miao, H. Wang, J. Tang, J. Am. Chem. Soc. 142 (2020) 2795–2802.
[35] S. Wang, M. Xu, T. Peng, C. Zhang, T. Li, I. Hussain, J. Wang, B. Tan, Nat. Commun. 10 (2019) 676.
[36] J. Arends, J.F. Verwey, Phys. Status. Solidi. B 23 (1967) 137–145.
[37] X. Li, Y. Sun, J. Xu, Y. Shao, J. Wu, X. Xu, Y. Pan, H. Ju, J. Zhu, Y. Xie, Nat. Energy 4 (2019) 690–699.
[38] C.M. Perez, D. Ghosh, O. Prezhdo, S. Tretiak, A.J. Neukirch, J. Phys. Chem. Lett. 12 (2021) 1005–1011.
[39] D. Mocatta, G. Cohen, J. Schattner, O. Millo, E. Rabani, U. Banin, Science 332 (2011) 77–81.
[40] J.S. Manser, P.V. Kamat, Nat. Photonics 8 (2014) 737–743.
[41] H. Li, J. Li, Z. Ai, F. Jia, L. Zhang, Angew. Chem. Int. Ed. 57 (2018) 122–138.
[42] P. Zhang, G. Zhang, L. Liu, D. Ju, L. Zhang, K. Cheng, X. Tao, J. Phys. Chem. Lett. 9 (2018) 5040–5046.
[43] Q.A. Akkerman, G. Rainò, M.V. Kovalenko, L. Manna, Nat. Mater. 17 (2018) 394–405.

[44] Z. Zhang, M. Wang, Z. Chi, W. Li, H. Yu, N. Yang, H. Yu, Appl. Catal. B: Environ. 313 (2022).
[45] H. Huang, J. Zhao, Y. Du, C. Zhou, M. Zhang, Z. Wang, Y. Weng, J. Long, J. Hofkens, J.A. Steel, M.B.J. Roeffaers, ACS Nano 14 (2020) 16689–16697.
[46] H. Rao, L.C. Schmidt, J. Bonin, M. Robert, Nature 548 (2017) 74–77.
[47] N. Sivasankar, W.W. Weare, H. Frei, J. Am. Chem. Soc. 133 (2011) 12976–12979.
[48] X. Yang, Y. Wang, C.M. Li, D. Wang, Nano Res. 14 (2021) 3446–3457.